Eng. Sci., 2025, **36**, 1658

Engineered Science
DOI: https://dx.doi.org/10.30919/es1658

Dynamic Heat Transfer and Thermal Storage Characteristics of Ultra-Thick Rammed Earth Walls under Summer Natural Ventilation on the Tibetan Plateau

Junjia Hu,[1,#] Xiaoliang Wang,[1,2,#] Li Yang,[1,2] Shuliang Li,[1,2] Yunke Yang,[1] Yuzhenru Sun,[1] Yong Sha,[3] Guanxing Pu[1] and Xianmin Mai[1,*]

Abstract

Traditional ultra-thick rammed earth walls in the Tibetan Plateau region show excellent thermal performance under extreme climatic conditions such as strong solar radiation, low-pressure hypoxia, and drastic temperature difference between day and night, but their dynamic heat transfer and energy regulation mechanism under the action of unsteady bidirectional thermal perturbation in the plateau still needs to be studied in depth. In this study, a three-dimensional unsteady two-way thermal coupling model of traditional rammed-earth dwelling walls in Shangri-La, Northwest Yunnan Province, was constructed based on the special climatic characteristics of the plateau, and the spatial and temporal heterogeneity law of heat transfer of the ultra-thick rammed-earth wall in summer and its heat storage/exothermic coupling mechanism were systematically elucidated. The results show that (1) the depth of influence of the external heat wave is 500 mm, and the depth of influence of the internal heat wave is 200 mm. (2) The standing wave node at the depth of 400 mm leads to the cyclic reversal of the direction of the heat flow, which delays the peak of the external temperature wave by 855 min (58.3% of the cycle), and the time lag of the extreme temperatures at different depths is predicted by the fitted function. (3) This wall can reduce interior temperature fluctuations by 73.6% to 77.5% through asymmetric heat transfer and high thermal storage properties, providing a core thermal buffer capacity for highland buildings. This study can provide a theoretical basis for dynamic thermal regulation of highland buildings to cope with climate extremes.

Keywords: Qinghai-Tibet plateau; Ultra-thick rammed Earth walls; Bidirectional thermal disturbances; Dynamic heat transfer; Spatial; Temporal properties.
Received: 13 May 2025; Revised: 22 July 2025; Accepted: 29 July 2025
Article type: Research article.

1. Introduction

Under the double pressure of frequent occurrence of global extreme climate events and energy crisis, the construction industry is facing the severe challenge of energy conservation and emission reduction.[1-2] Passive energy-saving technologies and high-performance building envelope design have become the core strategies to promote the development of green and low-carbon buildings.[3] The Tibetan Plateau, due to its unique high-altitude environment, intense solar radiation and drastic temperature difference between day and night, puts forward higher requirements on the thermal performance of building envelopes. Traditional ultra-thick rammed earth walls (over 700 mm thick) have demonstrated significant low-carbon adaptability in this region due to their excellent thermal inertia regulation.[4-6]

However, most of the existing studies focus on the structural performance of rammed earth walls,[7-9] and the quantitative analyses of their heat transfer characteristics and energy efficiency are still insufficient; and the numerical calculations and evaluation methods for the thermal characterisation of general wall systems are not directly applicable to the analysis of the heat transfer and storage characteristics of ultra-thick rammed earth walls under plateau climate conditions. Therefore, it is of great theoretical value and practical significance to systematically study the dynamic heat transfer mechanism of rammed earth walls under plateau climate through three-dimensional unsteady

---

[1] *School of Architecture, Southwest Minzu University, Chengdu, Sichuan, 610041, China*
[2] *Institute of Qinghai-Tibetan Plateau, Southwest Minzu University, Chengdu, Sichuan, 610041, China*
[3] *School of Chemistry and Environment, Southwest Minzu University, Chengdu, Sichuan, 610041, China*
[#] *These authors contribute equally*
[*] *E-mail:* maixianmin@foxmail.com (X.M. Mai)

Fig.1: Century-old Residence in Tangdui Village, Shangri-La, Diqing.

state numerical simulation methods, in order to optimise the thermal design of plateau buildings and promote the development of sustainable building technology.

This study focuses on the dynamic heat transfer and storage characteristics of rammed earth walls under natural ventilation conditions in summer, which is essentially a wall heat transfer process under the action of bidirectional harmonic waves. From the heat transfer theoretical perspective, the mechanism of this bidirectional temperature wave action is more complex and involves more general engineering practical problems.[10] In the traditional building thermal analysis, usually only simplified attention and indoor thermal environment is closely related to the internal surface temperature changes, while ignoring the internal temperature distribution and change rule of the wall - this simplified method in the conventional thickness of the wall system has applicability. However, the traditional simplified method cannot directly assess the thermal performance of ultra-thick rammed earth walls due to the difficulty of penetrating the wall itself by exogenous temperature waves and the significant influence of the indoor environment on the internal surface temperature under the natural ventilation conditions in summer. Therefore, in-depth analyses of the evolution of the internal temperature distribution and the heat storage and release characteristics of the wall are needed in order to provide theoretical guidance for practical engineering design.

With the continuous development of numerical simulation technology, significant progress has been made in the study of wall thermal performance. Traditional research primarily evaluated wall thermal performance using temperature time lag and decrement factor. Asan[11-13] employed the Crank-Nicolson scheme with periodic convective boundary conditions on the exterior surface to solve one-dimensional transient heat conduction equations, systematically investigating the effects of building material types, insulation layer thickness and position, and wall thermophysical properties on temperature lag and decrement factor. The results show that the thermal properties of building materials and the location of insulation play a crucial role in the thermal properties of walls. However, these methods are usually based on idealized assumptions of constant indoor temperatures and focus only on unidirectional outdoor thermal disturbances, which do not accurately characterize the effects of dynamic changes in the indoor environment of Tibetan Plateau residences on the thermal performance of walls.

In recent years, researchers have introduced new concepts such as “heat flux time lag” and “heat flux decreasing factor” to develop more sophisticated transient heat transfer models by coupling fluid, solid and radiation mechanisms. Xing Jin[14] proposed that the wall heat flux is a direct factor driving the indoor air temperature change, introduced these two metrics and analyzed their relationship with the thermophysical properties and thickness of the wall using a one-dimensional numerical model. C.R. Ruivo and P.M.

Table 1: Thermophysical Properties of Plateau Air and Wall Materials.

	$Pref$ (Kpa)	ρ (kg/m^3)	cp (J/kg·K)	λ (W/m·K)	μ (Pa·s)	Prt
AIR	71.6977	0.867	1043.18	0.0458	1.77508E-5	0.85
WALL	-	1942.64	1010.00	1.16	-	-

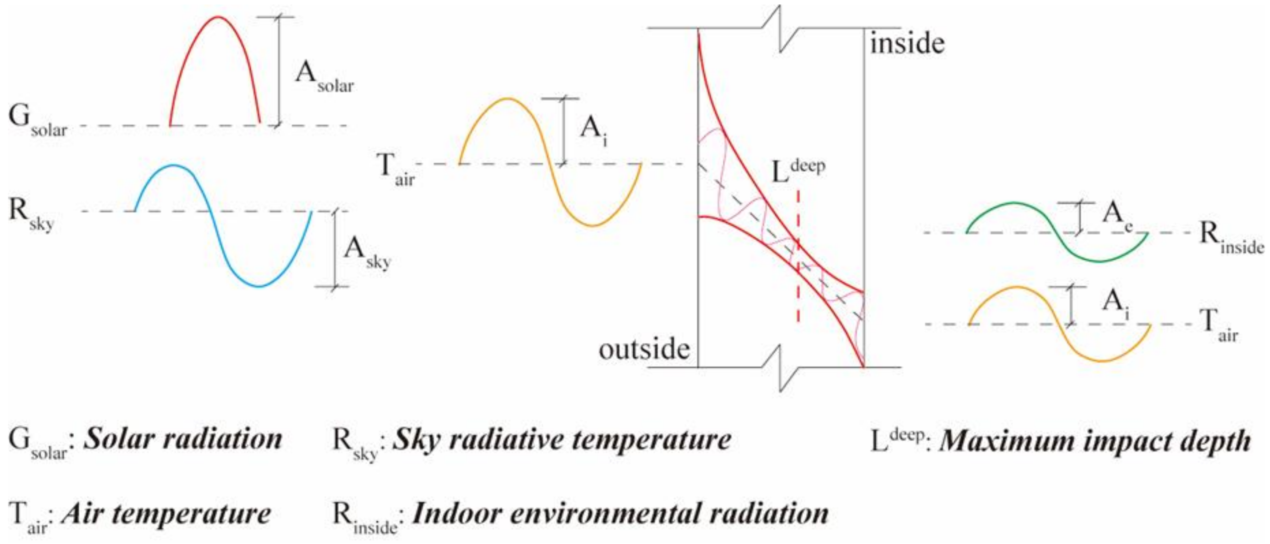

Fig. 2: Heat transfer mechanism of rammed earth wall under summer natural ventilation condition on plateau.

Ferreira[0] developed a transient heat transfer model by means of the finite difference method, using the solar-air temperature as an external boundary condition and assuming a constant internal temperature, and investigated the time lag and the diminishing factor of the heat flow through a multilayered wall, revealing their relationship with the wall color and orientation. D. Mazzeo[16] proposed a quantification method based on the attenuation factor of energy and heat flow with time lag in terms of the combined effect of external and internal air conditioning loads and evaluated the monthly and seasonal energy consumption of different wall structures under stabilization cycle conditions. In order to further explore the intrinsic mechanism of heat transfer in walls, Liting Yuan and Yihang Lu[17] calculated the heat flow attenuation factor and time lag of a single-layer wall based on the analytical method of auxiliary function, which proved that these parameters were governed by the diffusion length and thermal efficiency coefficient, providing new theoretical insights for optimization.

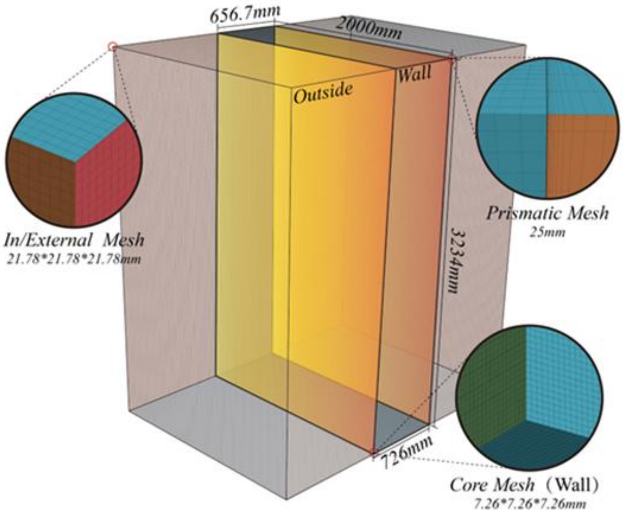

Fig. 3: Three-dimensional Geometric Model and Mesh Generation.

In addition, some of the studies have been extended to analyze the multidimensional performance of thermal inertness and energy storage. Sami A. Al-Sanea and M.F. Zedan[18] based on Riyadh climatic data and cyclic steady state conditions, proposed the "thermally inert energy saving potential" and "critical thermally inert thickness" and investigated the effect of thermal mass on insulated wall thermal performance and energy savings. Tugce Pekdogan and Tahsin Basaran[19] explored the thermal behavior of sandwich walls in dynamic thermal environments using an implicit finite difference method based on typical Turkish winter and summer meteorological data as external boundary conditions, and the results showed that sandwich walls show good climate adaptation by significantly reducing heat loss and heat gain in all climatic conditions. For the special needs of western China, where solar energy resources are abundant, Yan Liu and Liqiang Hou *et al*.[20] constructed a mathematical model of hollow masonry wall based on experimental validation, optimized and analyzed the effects of different structures on the energy efficiency of the wall, and finally proposed a suitable design scheme, which provides a theoretical basis for the promotion of this structure in practical applications.

In order to simplify the dynamic thermal performance characterization, Vincenzo Corrado and Simona Paduos[21-22] proposed two evaluation metrics, "equivalent steady state heat transfer rate" and "equivalent periodic heat transfer rate", and based on the conduction transfer function method to verify their applicability under periodic boundary conditions. N.C. Balaji and Monto Mani[23] analyzed the thermal properties of homogeneous and composite walls using finite difference and incidence methods, explored the effects of thermal incidence, decay factor, heat capacity and thermal conductivity on the time lag and decay factor, and revealed the key role of different material thermal properties in optimizing the thickness of walls. Francesco Leccese and Giacomo Salvadori[24] further investigated the effect of the positioning and thickness

Table 2: Measured Average Solar Radiation in Different Directions on the Summer Solstice in Shangri-La.

North	South	West	East	Horizontal Plane	Unit
299.31	242.10	211.68	492.51	844.68	W/m^2

distribution of insulation materials on the dynamic thermal performance and proposed a modified formulation based on the heat transfer matrix method, which provides a simplified solution for modeling dynamic thermal behavior. In terms of experimental studies, Pushpendra Kumar Singh Rathore and Shailendra Kumar Shukla[25] evaluated the moderating effects of phase change materials on indoor temperature peaks, thermal amplitudes, time lags, and attenuation coefficients by conducting a year-long field experiment in a zone of peak energy-saving potential for a tropical climate, and analyzed their effects on cooling loads and average annual heat flow.

Limitations of Existing Studies:

(1) Conventional numerical models often oversimplify boundary conditions as steady-state or homogeneous parameters, inadequately capturing dynamic plateau climate features such as low pressure, intense radiation, and drastic diurnal temperature fluctuations.

(2) Research predominantly focuses on standard-thickness walls, with insufficient quantification of nonlinear heat transfer behaviors and energy storage-release hysteresis induced by enhanced thermal inertia in ultra-thick rammed earth walls.

To address the limitations of existing research, this study develops a three-dimensional unsteady two-way thermal coupling model for ultra-thick rammed earth walls under bidirectional thermal disturbances on the Qinghai-Tibet Plateau, based on summer solstice field measurement data from Shangri-La, Yunnan, using the finite volume method. The model couples multi-source dynamic boundary conditions, including indoor-outdoor air convection, environmental long-wave radiation, and solar short-wave radiation. By discretizing and solving the energy conservation equation, high-precision numerical simulation of the spatiotemporal evolution of the temperature field within the wall is achieved. This study aims to reveal the dynamic thermal response mechanisms of ultra-thick rammed earth walls under natural ventilation conditions in summer, including temperature decay, time lag characteristics, and the dynamic balance between energy storage and release. The results of the study not only provide a theoretical basis for the design of rammed earth walls for highland buildings, but also provide innovative insights into the development of sustainable building technologies in extreme climatic regions.

This study consists of three main parts:

(1) Construct a three-dimensional dynamic heat transfer simulation model for ultra-thick rammed earth walls;

(2) Validation of the simulation accuracy of the 3D dynamic simulation model under summer environmental conditions and establishment of corresponding evaluation indexes;

(3) Analyze the temporal and spatial variation rules of the temperature field of the wall under two-way thermal perturbation and the heat storage and release characteristics.

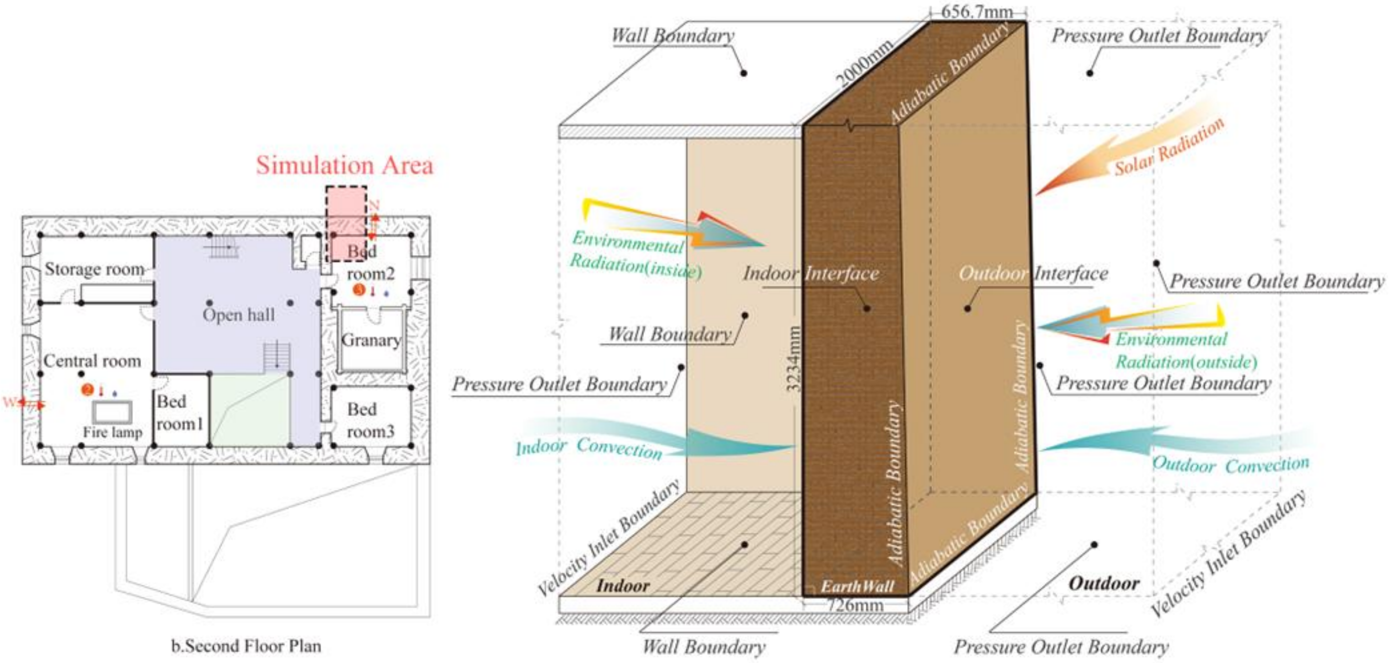

Fig. 4: Simulation Area and Physical Model Boundary Setup.

Table 3: Static Accuracy Verification of Numerical Simulation Results.

Metric / Parameter	Exterior Surface	Interior Surface	Acceptance Criteria
RMSE	0.763°C	0.251°C	＜1°C (Qualified)
R^2	0.965	0.915	＞0.9 (Excellent)
Mean AE	0.62°C	0.20°C	＜1°C (Qualified)
Max AE	1.32°C	0.73°C	＜2°C (Qualified)

2. Research objects and methods

2.1 Study focus and heat transfer mechanism

2.1.1 Study focus

In order to study the heat transfer and heat storage characteristics of ultra-thick rammed earth walls on the Tibetan Plateau, a century-old residential house in Tangdui Village, Shangri-La City, northwest Yunnan Province (Fig.1) was selected for this study. In order to avoid uncontrollable differences in subsequent model validation due to variations in direct solar radiation fluxes influenced by cloud conditions, which are more difficult to reproduce completely at the simulation level, the north-facing wall measurement point of the building was thus selected for analysis in this simulation.

Definition of the study scope and environmental boundary conditions:

In view of the significant difference in thermal properties between ultra-thick rammed earth walls and traditional wall systems, it is difficult for external thermal perturbations to penetrate the walls, thus creating better thermal stability, and the maximum penetration depth of external thermal perturbations under extreme conditions is of great theoretical significance for the determination of indicators such as the thickness of rammed earth residential wall construction in plateau regions. This study focuses on the heat transfer and storage characteristics of rammed earth walls under natural ventilation conditions in summer: since the effect of radiation on the surface temperature change of the wall is significantly stronger than that of convection, a 48-hour climate data set measured on the summer solstice, which can represent the strongest radiation scenario in the summer, is selected as the boundary condition to obtain the maximum depth of penetration of thermal perturbation in summer. It should be noted that the indoor temperature can only be maintained at 2-3°C in winter under natural ventilation conditions, which fails to meet the comfort demand, so the temperature and humidity need to be constant at 18°C through indoor heating. For this reason, the maximum depth of penetration under extreme winter conditions will not be discussed in this paper and will be studied independently by constructing a one-way thermal perturbation model.

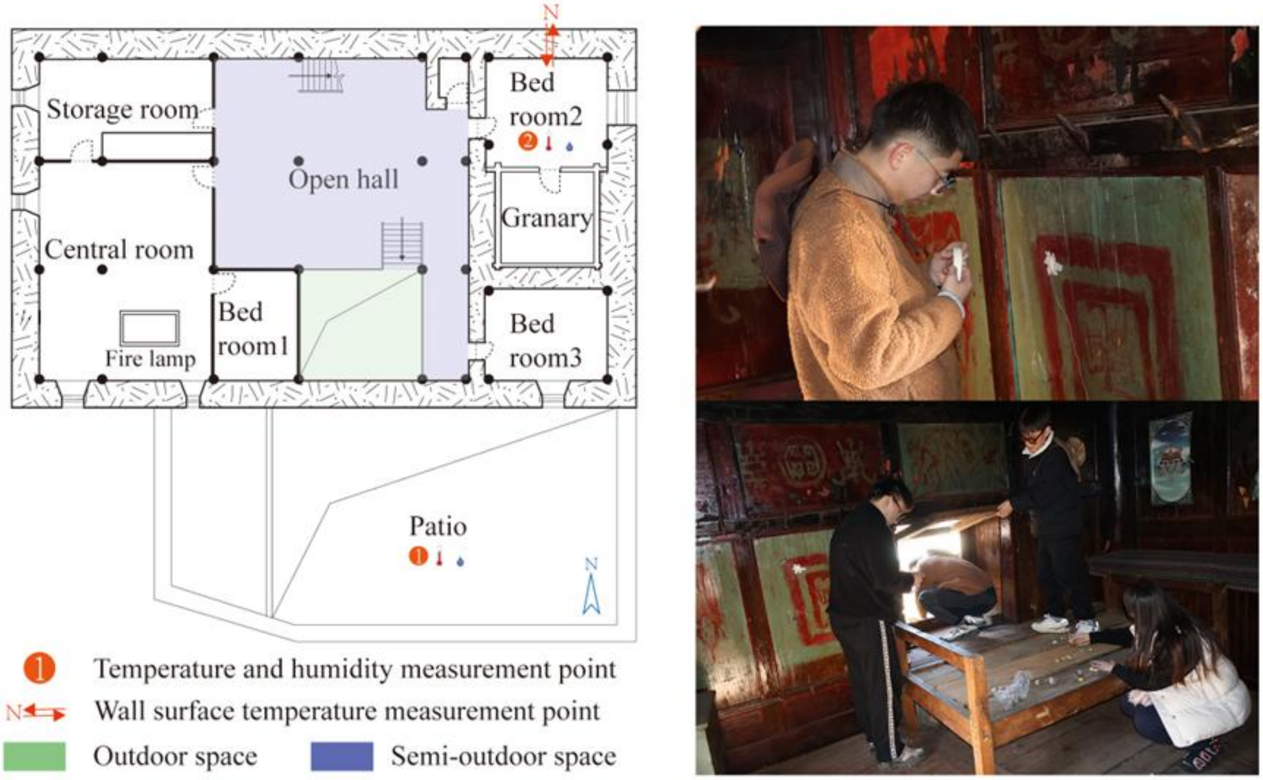

a.Second Floor Plan b.Layout of Measuring Points

Fig.5: Layout of Field Measurement Points for Climatic Environment on the Summer Solstice in Century-Old House.

Table 4: Dynamic Accuracy Validation of Numerical Simulation Results.

Metric / Parameter	Exterior Surface	Interior Surface	Acceptance Criteria
PD	0min	Lag 9 min	＜15min (Qualified)
PTD	0min	Lag 10 min	＜15min (Qualified)

2.1.2 Heat transfer mechanism

The dynamic heat transfer and storage characteristics of a rammed earth wall under natural ventilation in summer, which is targeted in this study, is essentially the wall heat transfer under the action of bidirectional harmonics (Fig.2). This bidirectional harmonic originates from the periodic thermal perturbation coupling between the external and internal environments: in the external environment, solar radiation; sky radiant temperature; and air temperature together constitute the external thermal harmonic source. In the internal environment, the dynamic fluctuation law of indoor air temperature and environmental radiation under natural ventilation conditions forms the internal thermal harmonic source. The bidirectional harmonics act alternately through the wall surface to drive the heat transfer in both directions inside and outside the wall, forming a dynamic heat transfer and storage process.

It is worth emphasising that the maximum depth of influence L^{deep} in the figure reveals the effective range of temperature waves inside the wall - for ultra-thick rammed earth walls (thickness over 700 mm), the penetration ability of external thermal harmonics is limited, and it is difficult for the temperature waves to penetrate completely through the wall; at the same time, internal thermal harmonics are affected by the dynamic changes of the indoor environment under natural ventilation, which leads to the traditional simplified analysis that only focuses on the internal surface temperature, and cannot accurately reflect the real thermal state distribution inside the wall. Therefore, the heat transfer mechanism under the action of bidirectional harmonics needs to focus on the spatial and temporal evolution of the temperature field inside the wall and the spatial and temporal coupling of the heat storage and release processes, which is of key theoretical value for analysing the thermal performance of ultra-thick rammed earth walls in plateau climate.

2.2 Numerical modeling framework

In order to accurately characterize the dynamic thermal response of ultra-thick rammed earth wall under bidirectional thermal perturbation in plateau climate, a three-dimensional dynamic numerical simulation model based on STAR-CCM+ multiphysics field coupling platform was established in this study. The model comprehensively considered the dynamic coupled heat transfer effect under the environmental and climatic characteristics of the Tibetan Plateau, such as high altitude (2903.00 m), low pressure (71.70 kPa), and strong solar radiation (844.68 W/m²), and the measured indoor and outdoor thermal environment data were used to determine the dynamic boundary conditions.

2.2.1 Geometric modeling and meshing strategy

Based on the measured structural data of traditional rammed earth dwellings in Shangri-La, Yunnan, a parameterized three-dimensional geometric model was constructed in the STAR-CCM+ platform at a 1:1 scale (Fig.3). The model comprises three computational domains:

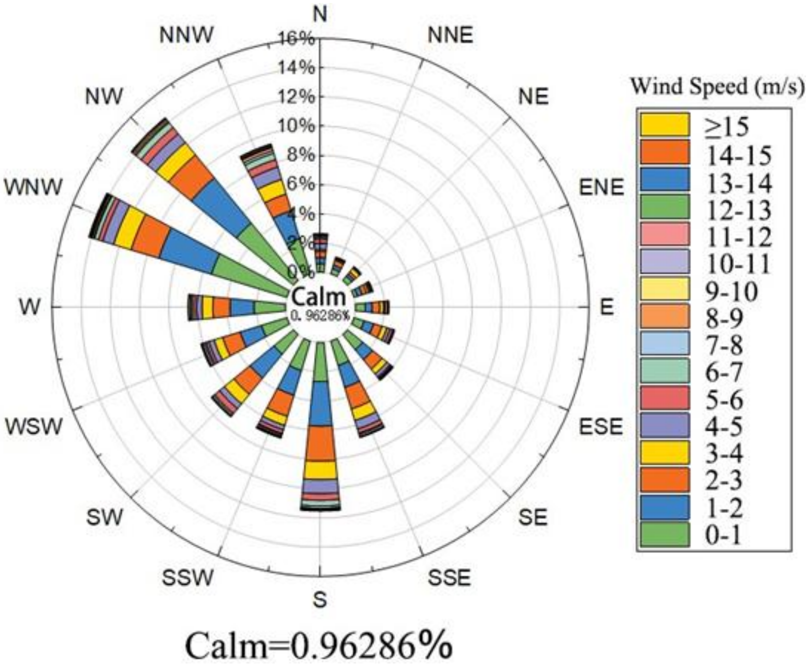

Fig. 6: Summer Outdoor Wind Rose Diagram of Shangri-La.

Table 5: Equivalence analysis of temperature decay of equal-thickness and non-equal-thickness walls.

$f_{probe}^{\text{Phase I}}$	PROBE 1-2	PROBE 2-3	PROBE 3-4	PROBE 4-5	PROBE 5-6	PROBE 6-7	PROBE 7-8
Non-uniform thickness wall	-0.47	-0.85	0.71	0.73	0.61	0.54	0.52
Uniform thickness wall	-0.49	-0.86	0.74	0.73	0.63	0.51	0.51
Absolute difference	2%	2%	3%	0	2%	3%	1%

(1) Rammed Earth Wall Domain: Dimensions of 2000 mm (width) × 3234 mm (height) × 726 mm (depth), linearly tapered to 656.7 mm at the top, forming a trapezoidal cross-section with a 1.2° inclination;

(2) Indoor Air Domain: Located adjacent to the interior wall surface, dimensions of 2000 mm (width) × 3234 mm (height) × 1000 mm (depth), designed to simulate natural convection boundary conditions with sufficient depth for fully developed flow;

(3) Outdoor Air Domain: Positioned exterior to the wall, conforming to the tapered outer surface, with identical dimensions to the indoor air domain.

A multi-scale non-uniform meshing strategy was applied to the three computational domains as follows (Fig. 3):

(1) The core rammed earth wall domain was discretized using cut-cell meshes with a grid size of 7.26 mm, totaling 11.76 million cells.

(2) Indoor/outdoor air domains employed hybrid meshes combining cut-cells and boundary layers, containing 0.92 million elements. Target grid cells maintained isotropy with a characteristic size of 21.78 mm (≈3% of wall thickness). Additionally, 20 boundary layer grids with a total thickness of 25.0 mm were deployed at the wall-air interfaces to ensure thermal gradient resolution accuracy.

(3) Mesh diagnostics: Global mesh topology validity was verified against ASME V&V 20-2009 standards[26], achieving orthogonality >0.85, skewness <0.7, zero negative-volume cells, 100% face validity, and 99.98% volume conservation.

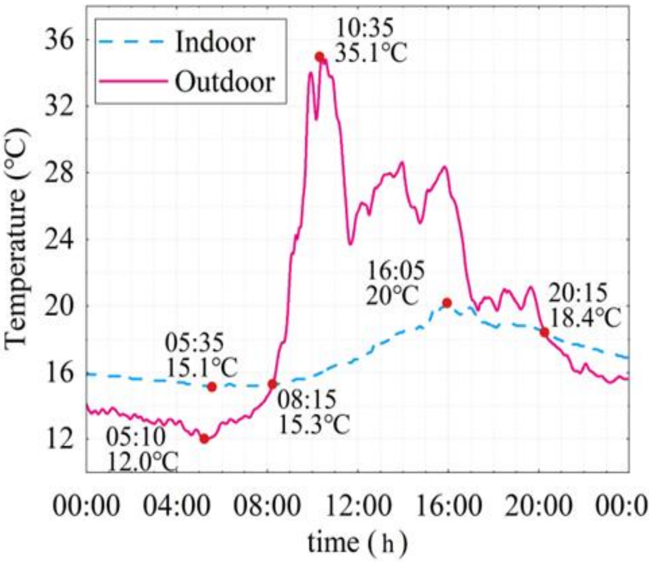

Fig. 7: Measured Indoor and Outdoor Air Temperatures of a Century-Old House on the Summer Solstice Day.

2.2.2 Governing equations and boundary conditions

This study establishes a three-dimensional unsteady thermal response mathematical model for plateau rammed earth walls by coupling fluid, solid, and radiative heat transfer mechanisms. The specific configurations are as follows:

(1) Fluid Domain Momentum Equation: Airflow is governed by the Realizable k-ϵ turbulence model[27] Eq. (1):

$$\rho_0\left(\frac{\partial v}{\partial t}+\nabla \mathrm{v}\cdot \mathrm{v}\right)=-\nabla p+\nabla\cdot[(\mu+\mu_t)(\nabla v+\nabla v^T)] \\ +\rho_0\beta(T-T_{ref})g \tag{1}$$

Where $\mu_t=\rho C_\mu k^2/\epsilon$ is turbulent viscosity. The Boussinesq approximation uses $\rho_0=0.8\mathrm{kg/m^3}$ to model natural convection under low-pressure conditions.

(2) Fluid Domain Energy Equation: Couples conduction and turbulent transport[27] Eq. (2):

$$\frac{\partial}{\partial t}(\rho C_pT)+\nabla\cdot(\rho C_pvT) \\ =\nabla\cdot\left(\left(k+\frac{\mu_tC_p}{Pr_t}\right)\nabla T\right) \tag{2}$$

with turbulent Prandtl number $Pr_t=0.85$. Temporal discretization employs a second−order implicit scheme (Δt =5min, 20 iterations per step), constrained by Courant number<1.0.

(3) Radiative transfer: Integration of solar radiation, sky longwave radiation and surface-to-surface (S2S) radiation exchange[28] Eq. (3):

$$\rho C_p\frac{\partial T}{\partial t}=\nabla\cdot(k\nabla T)+\alpha_{WALL}G_{SOLAR}\cos\theta+\epsilon_{WALL}\sigma \\ \left(T_{SKY}^4-T_{WALL}^4+\sum_{j=1}^{N}F_{j\to WALL}\varepsilon_jT_j{}^4\right) \tag{3}$$

Where G_{SOLAR} is computed dynamically via a solar calculator[29] at coordinates 27.993877°N, 99.549141°E. Surface-to-surface radiation uses gray-body assumption ϵ_{WALL} and view factor tracing($F_{j\to WALL}$).

(4) Boundary Conditions:

As shown in Fig. 4, the total heat flux on the exterior surface consists of convective heat transfer, solar radiation, sky long-wave radiation and surface-to-surface (S2S) radiation exchange, and its mathematical expression is shown in Eq. (4); while the total heat flux on the interior surface

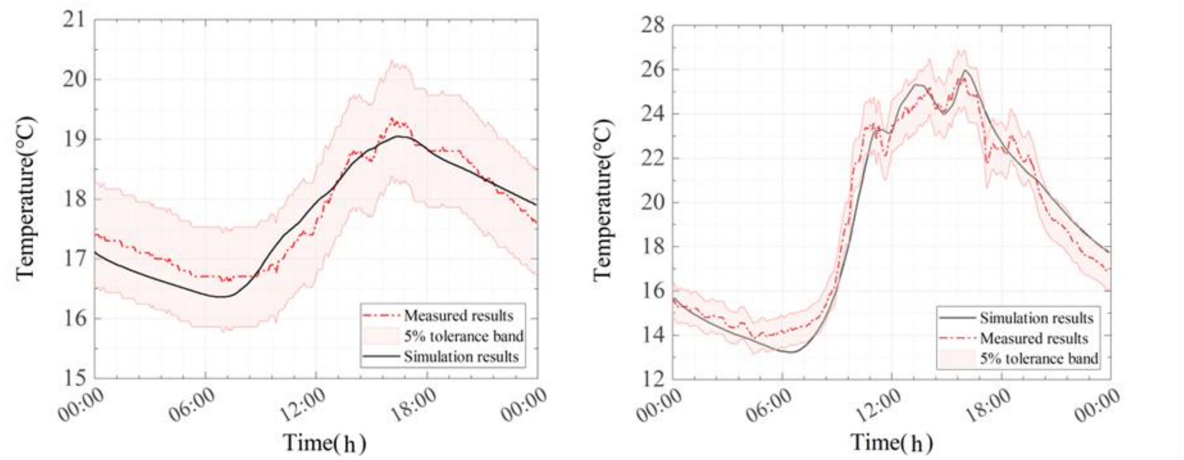

(a) interior surface (b) exterior surface

Fig. 8: Comparison and Validation Figure of Measured and Simulated Interior and Exterior Surface Temperatures on the North Wall of Century-old Residence.

consists of convective heat transfer and S2S radiation exchange.

$$\begin{aligned} -k\frac{\partial T}{\partial t} &= h_{conv}(T_{WALL} - T_{AIR}) \\ &\quad + \alpha_{WALL} G_{SOLAR} \cos\theta \\ &\quad + \epsilon_{WALL}\sigma(T_{SKY}^4 - T_{WALL}^4) \\ &\quad + \sum_j f_{j\rightarrow WALL}\varepsilon_j\sigma\left(T_j^4 - T_{WALL}^4\right) \end{aligned} \tag{4}$$

Boundary conditions for the outdoor air calculation domain: A configuration scheme with one velocity inlet and four pressure outlets is used. Among them, the temperature parameters of the velocity inlet are input into the 48-hour field measurement data set of outoor temperature through the field function table, the flow rate is set to be a north-westerly wind of 2 m/s, and the convective heat transfer coefficient (h_{conv}) is automatically calculated by the program; the temperature parameters of the pressure outlets are kept the same as those of the velocity inlet. For radiative transfer, solar radiation is calculated automatically by entering latitude, longitude, time, diffuse flux fraction and sunlight factor in the solar calculator, ensuring that its radiation value coincides with the measured average solar irradiance in Table 2; sky radiation follows $T_{sky} = T_{\infty,0}\left(0.8 + \frac{T_{dp}}{250}\right)^{0.25}$ [30], calculated by intervening in the grey-body radiative transfer integral through a user-defined boundary radiation field.

Boundary conditions for the indoor air computational domain: A configuration with one velocity inlet, one pressure outlet and three wall conditions is used to simulate the indoor environment. The temperature parameter of the velocity inlet is input into the 48-hour indoor temperature field measurement data set through the field function table, and the flow rate is set to 0.5 m/s to ensure the numerical stability of the indoor convection term; the temperature parameter of the pressure outlet is the same as that of the velocity inlet. The indoor ambient thermal radiation is input into the 48-hour indoor temperature field measurement dataset approximating the indoor radiant temperature through the field function to intervene in the grey body radiative transfer integral calculation.

2.2.3 Material properties and steady-state initialization

Based on the measured wall density of 1942.64 kg/m³ and referencing the thermophysical properties of compacted clay materials with a density of 2000 kg/m³ from the Thermal Design Code for Civil Buildings (GB50176-2016),[31] the thermal properties of the wall material are defined as follows (Table 1).

The thermophysical properties of plateau air were calculated using the Engineering Tool Box[32], based on field-measured average temperature-humidity data, altitude of 2903 m, and mean atmospheric pressure of 71.6977 kPa, as shown in Table 1.

Based on the radiation absorption coefficient of 0.48 for white lime plastered walls specified in the Chinese National

Table 6: Temperature Fluctuation Amplitudes and Temperature Attenuation Factors.

	Probe1 (700mm)	Probe2 (600mm)	Probe3 (500mm)	Probe4 (400mm)	Probe5 (300mm)	Probe6 (200mm)	Probe7 (100mm)	Probe8 (0mm)
$A_{probe}^{\text{Phase I}}$	2.68	1.32	1.13	1.52	2.09	3.32	6.49	12.77
$f_{probe}^{\text{Phase I}}$	0.49	0.86	0.74	0.73	0.63	0.51	0.51	

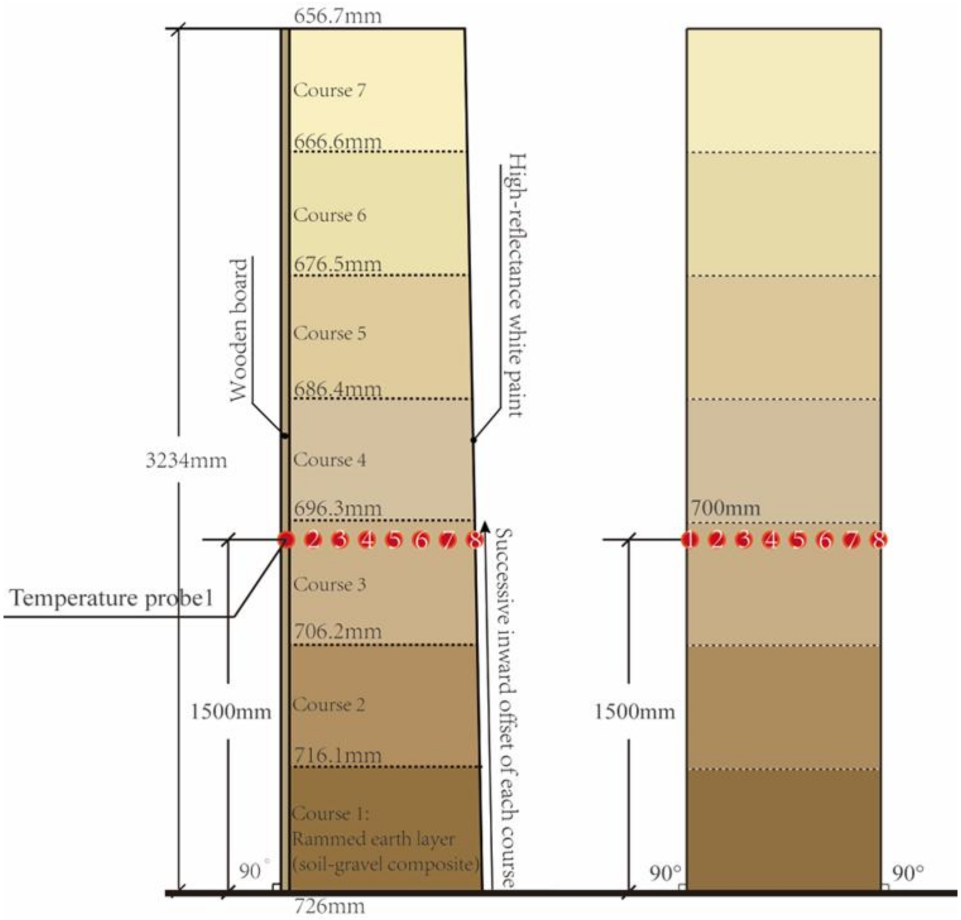

Fig. 9: Structural dimensions of equal-thickness and non-equal-thickness walls and placement of probe points.

Standard GB 50176-2016 "Code for Thermal Design of Civil Buildings",[31] the exterior surface emissivity is defined as $\epsilon_{out} = 0.48$, while the interior surface emissivity $\epsilon_{in} = 0.65$ is determined according to wood's radiation absorption characteristics. To ensure unimpeded environmental and solar radiation interactions on the exterior wall surface, all outdoor boundaries are assigned fully transparent radiation properties. To eliminate interference from internal surface radiation on heat transfer at the inner wall, indoor boundaries are defined as fully reflective.

Furthermore, to accurately simulate heat flux and temperature dynamics within the wall under bidirectional thermal disturbances while avoiding transient simulation distortions caused by uniform initial temperature assumptions[33], a steady-state preheating procedure is implemented. Using measured initial wall surface temperatures (interior: 17.4°C; exterior: 15.5°C) from the 24-hour transient simulation, steady-state heat conduction is solved with a convergence criterion of energy residuals below 1.0×10^{-4}. The resultant quasi-equilibrium temperature field serves as the initial condition for subsequent transient simulations.

2.3 Basic analytical metrics

Two indicators, attenuation factor and time lag, are usually used to evaluate the dynamic thermal performance of walls:

(1) Attenuation factor f: Defined as the ratio of thermal wave amplitude attenuation during propagation, calculated by Eq. (5)[13]:

$$f = A_{inner}/A_{outer}(0 \leq f \leq 1) \tag{5}$$

where A_{inner}: amplitude of inner surface temperature fluctuations; A_{outer}: amplitude of outer surface temperature fluctuations.

(2) Time lag φ: Defined as the temporal difference between the arrival of thermal waves at the inner and outer surfaces, calculated by Eq. (6)[13].

$$\varphi = \tau_{T_{max}^{inner}} - \tau_{T_{max}^{outer}} \tag{6}$$

where $\tau_{T_{max}^{inner}}$: time when inner surface temperature reaches its maximum; $\tau_{T_{max}^{outer}}$: time when outer surface temperature reaches its maximum.

In this study, due to the difficulty of outdoor heat waves fully penetrating the rammed earth wall, and under bidirectional thermal perturbation boundary conditions, the two traditional indicators of attenuation factor and time lag cannot be directly used to assess the dynamic thermal performance of the wall, necessitating targeted optimization research. Based on this, this study optimizes and improves the "attenuation factor" and "time lag effect", and proposes a new evaluation index applicable to rammed earth walls—

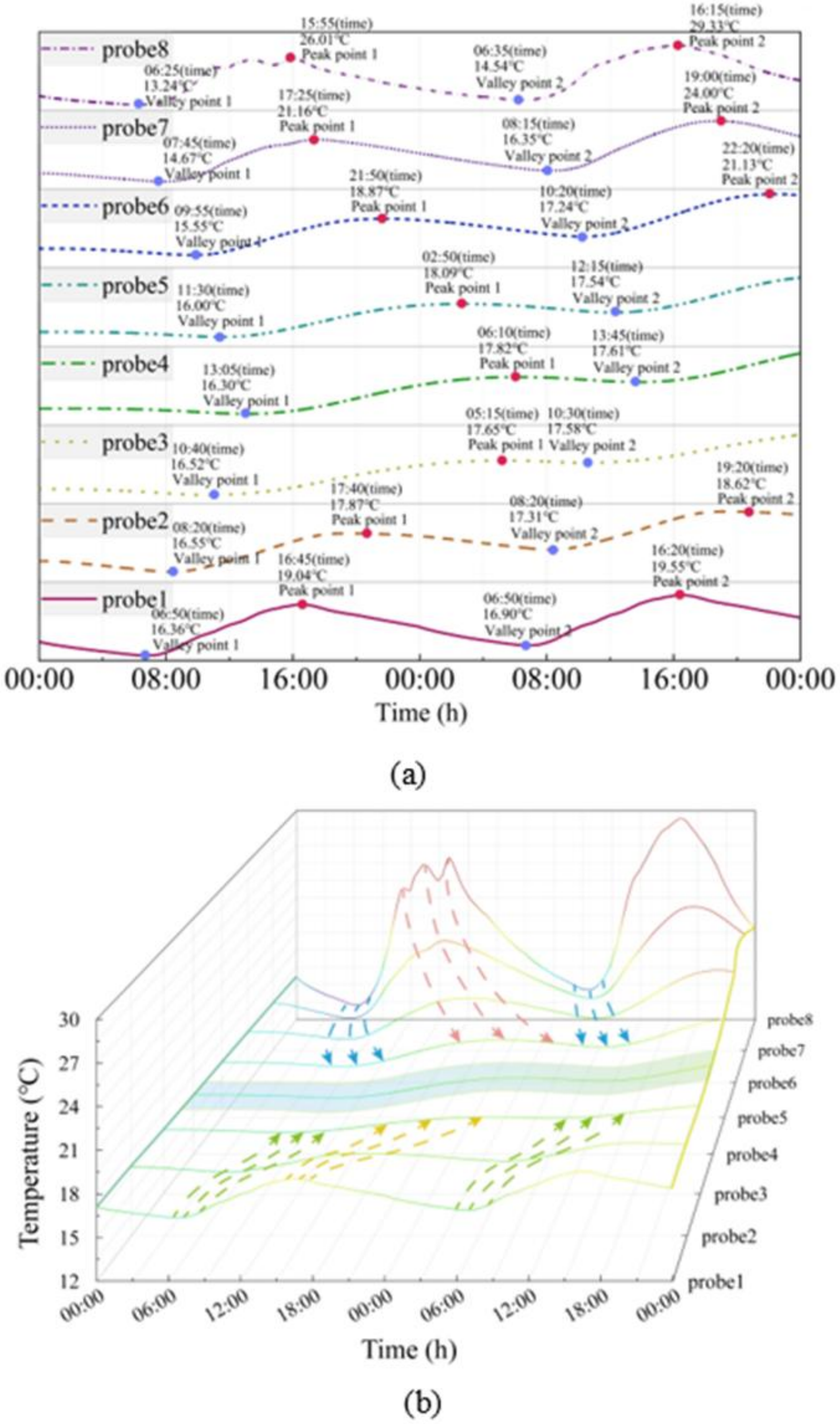

Fig. 10: Spatiotemporal Visualization Series of Temperature Field in Rammed Earth Walls under Bidirectional Thermal Disturbance (48-Hour).

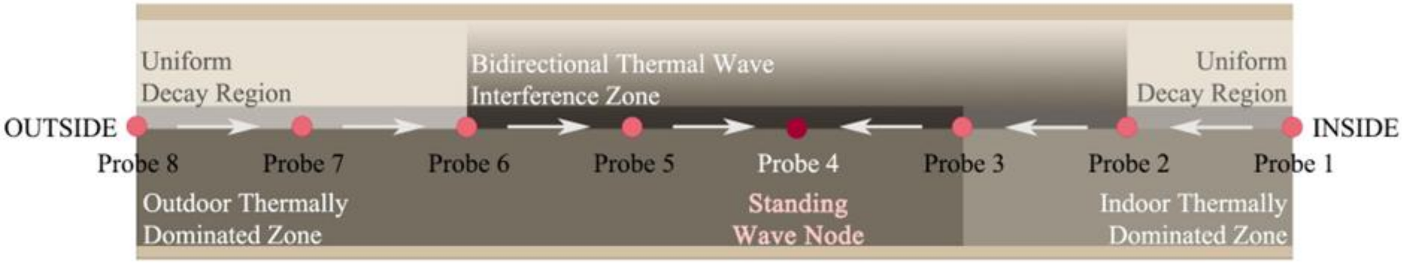

Fig. 11: Partitioning of Heat Transfer Characteristic Zones in Walls.

"maximum impact depth", as follows:

(1)"Attenuation factor"$f_{probe}^{\text{Phase I}}$: defined as the proportion of attenuation of the bi-directional heat wave amplitude during propagation with respect to the temperature of the detection point at different depths, calculated by the following formula Eq. (7).

$$f_{probe\ out-in}^{\text{Phase I}} = A_{probe\ out}^{\text{Phase I}} / A_{probe\ in}^{\text{Phase I}} (0 \leq f \leq 1) \tag{7}$$

Where: $A_{probe\ out}^{\text{Phase I}}$: the amplitude of the first cycle temperature fluctuation at the shallow measurement point; $A_{probe\ in}^{\text{Phase I}}$: the amplitude of the first cycle temperature fluctuation at the deep measurement point.

(2) "Time lag effect "k^{peak}: defined as the time lag effect at different depth detection points, calculated as follows Eq. (8).

$$k^{peak} = {\varphi_{L_{out-in}}}^{peak} / L \tag{8}$$

Where: ${\varphi_{L_{out-in}}}^{peak}$ is the time lag of the peaks at different measurement points from shallow to deep; L is the depth spacing between two detection points.

(3)"Maximum impact depth" L^{deep} : defined as the maximum impact depth of the exogenous heat wave in the rammed earth wall, by which the matching between the wall thickness and the dynamic thermal performance can be roughly judged. This indicator should be combined with the internal temperature field distribution, temperature decay, and time lag for comprehensive characterization.

2.4 Model simplification and validation

In order to fully consider the boundary thermal effect of summer plateau climatic conditions and accurately simulate the dynamic thermal response characteristics of ultra-thick rammed earth walls, this study adopted the testing method specified in the "Standard for Testing Methods of the Thermal Environment of Buildings" (JGJ/T347-2014) [0], and obtained field-measured climatic datasets during the summer solstice period (21–23 June 2023), including indoor and outdoor temperatures, indoor wind speeds, outdoor wind speed and direction, outdoor solar radiation, and sky radiation, which served as dynamic boundary conditions for numerical simulation of heat transfer (Fig. 5).

In summer, the dominant outdoor wind direction is northwest wind, and the wind speed is mainly between 0 and 3 m/s, and the indoor is basically calm (Fig. 6). The outdoor temperature fluctuated drastically during the day and night, and the temperature difference between day and night could be as high as 23.1°C. The natural regulation of the building greatly attenuated the indoor temperature variation, and the average daily indoor temperature was 17.5°C, and the difference between day and night was reduced to 4.9°C, which indicated that the indoor ambient temperature was comfortable. The daily minimum values of outdoor and indoor temperatures were 15.1°C and 12°C at 05:35 AM. and 05:10 AM., respectively, and the maximum values were 35.1°C (outdoor) and 20°C (indoor) at 10:35 AM. and 16:05 PM. In addition, the curves of indoor and outdoor temperatures intersected at 08:15 AM. and 20:15 PM (Fig. 7).

There were significant differences in the average solar radiation intensity in all directions outside (Table 2): the horizontal plane had the highest average radiation intensity of 844.68 W/m^2, indicating that this area receives the highest concentration of solar radiation. The average radiation intensity in the eastern direction was the next highest at 492.51 W/m^2, showing the significant effect of morning solar radiation. The mean radiation intensity in the north-south direction was 299.30 W/m^2 and 242.10 W/m^2 respectively, reflecting the significant effect of building orientation on the distribution of solar radiation. The lowest average radiation intensity of 211.68 W/m^2 was observed in the west direction, which was mainly related to the lower solar altitude angle in the afternoon and the shading by clouds or mountains.

2.4.1 Experimental validation of simulation data

In the following, a graphical comparison (Fig. 8) and multidimensional accuracy analysis will be conducted between the dynamic simulation data and field-measured data for the interior and exterior surfaces of the north-facing wall

Static accuracy validation was conducted for the root mean square error (RMSE) Eq. (9), coefficient of determination (R²) Eq. (10), mean absolute error (Mean AE), and maximum absolute error (Max AE) of the interior and exterior surface temperature predictions, as detailed in Table 3.

$$RMSE = \sqrt{\frac{\sum_{i=1}^{n}\left(X_{obs,i} - X_{modle,i}\right)^2}{n}} \tag{9}$$

$$R^2 = 1 - \frac{\sum_{i=1}^{n}(y_i - \hat{y}_i)^2}{\sum_{i=1}^{n}(y_i - \bar{y})^2} \tag{10}$$

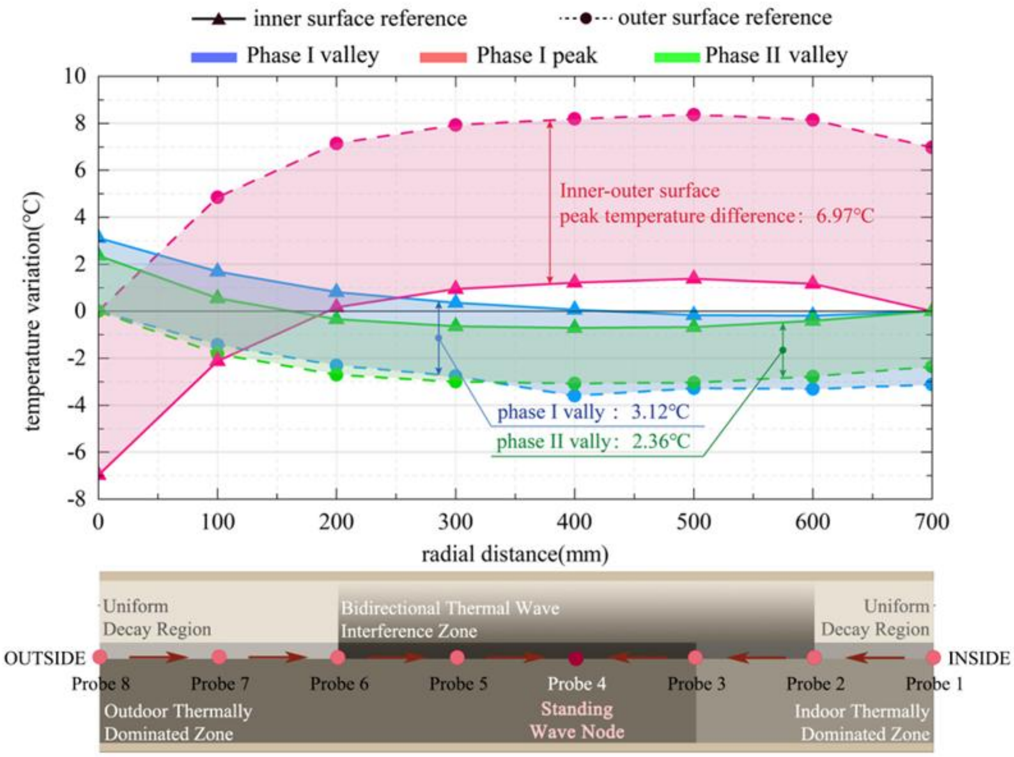

Fig. 12: Temperature Difference-Depth Profile Analysis Diagram.

The results indicate that the root mean square error (RMSE) of exterior surface temperature predictions is 0.763°C, with a coefficient of determination (R^2) of 0.965, demonstrating that the model explains 96.5% of the measured temperature variations. The maximum absolute error of 1.32°C remains within acceptable tolerance limits. Interior surface predictions exhibit superior accuracy, achieving an RMSE of 0.251°C and R^2 of 0.915, with 90% of errors confined to a ±0.3°C range. These metrics validate the accuracy of the three-dimensional numerical model in simulating temperature and heat transfer dynamics.

Additionally, dynamic accuracy verification was conducted for the phase difference (PD) and peak time difference (PTD) between simulated and measured temperatures on both surfaces of the north-facing wall (Table 4). The results show that the exterior surface temperature fluctuations are fully synchronized with the measured data. Although a 9-minute lag exists for the interior surface, this lag is significantly better than the acceptable threshold of 15 minutes, demonstrating the model's effectiveness in characterizing the wall's thermal storage behavior.

2.4.2 Model simplification and equivalence analysis

The structural system of this building's locally rammed earth wall is characterised by a systematic layering as a central feature, achieving stable mechanical properties through layered construction (Fig. 9). The thickness of the base layer is 726 mm, and the structural grading is achieved by layered rammed earth, with the height of the formwork for each layer being controlled at 467-600 mm. the outer side is increased by 10 mm for each layer, while the inner side is maintained in a vertical configuration, resulting in a trapezoidal cross-section that is wide at the bottom and narrow at the top. This tapered configuration improves lateral stiffness by lowering the center of gravity of the wall and reduces the shear stress on the foundation by the upper self-weight, which is crucial for the structural stability of the rammed earth wall.

It is important to note that the uneven thickness of the wall due to the battering system will have some impact on the definition of the wall thickness and the evaluation of the thermal characteristics. Therefore, this section will compare and analyse the heat transfer and storage equivalence of equal-thickness and non-equal-thickness rammed earth walls.

In order to compare the equivalence of equal-thickness and non-equal-thickness walls, based on the model verified in the previous section, the geometric parameters were modified to 700 mm equal thickness, and eight temperature probes were uniformly arranged along the radial depth of the two types of walls at a height of 1.5 m (at the thickness of 700 mm) (Fig. 9) to simulate the temperature fields of the 700-mm equal-thickness wall and the battered wall, respectively. Subsequent analyses will focus on equivalence analysis of internal temperature attenuation and inner/outer surface heat flux.

Equivalence analysis of temperature attenuation coefficients: The temperature attenuation coefficients between different detection points inside the two walls were calculated based on Eq. (7). Comparison shows that the temperature attenuation trend and direction are highly consistent; the absolute difference in attenuation coefficients between equal-thickness and non-equal-thickness walls is 1–3%, which is less

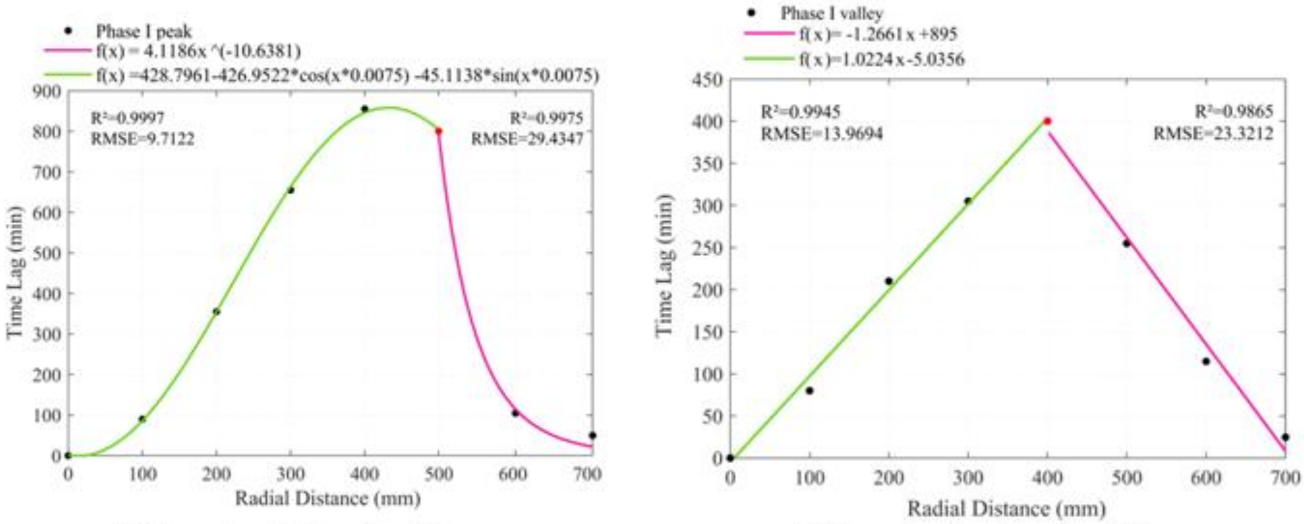

(a) Phase I peak Function Fitting. (b) Phase I valley Function Fitting.

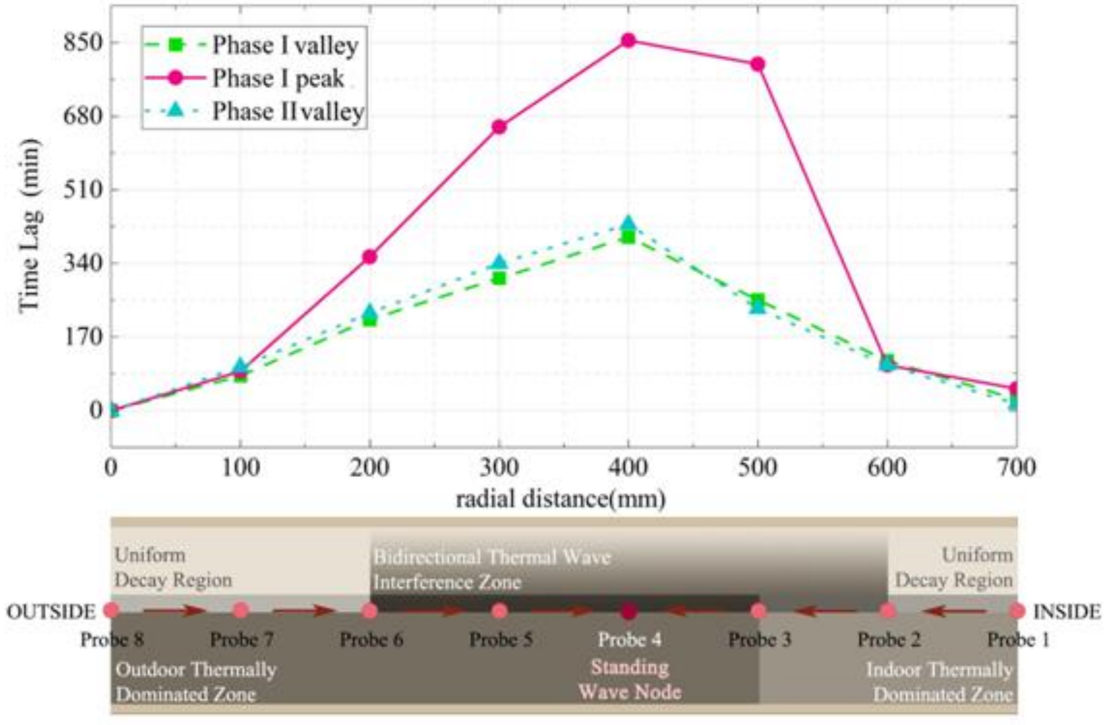

(c) The Time Lag - Depth Profile Analysis Diagram.

Fig. 13: The Time Lag Characteristics of Extreme Temperatures at Different Measurement Points on the Wall and Function Fitting.

than 5% in all adjacent detection points (Table 5).

Equivalence analysis of heat flow on internal and external surfaces: The results of heat flow on internal and external surfaces show that: the inflow on the internal surface of the non-equal-thickness wall is 0.164kWh/m², the outflow is 0.070kWh/m²; the inflow on the internal surface of the equal-thickness wall is 0.158kWh/m², and the outflow is 0.063kWh/m². For non-equal-thickness walls, the inflow on the outer surface is 0.894kWh/m² and the outflow is 0.490kWh/m²; for equal-thickness walls, the inflow on the outer surface is 0.930kWh/m² and the outflow is 0.444kWh/m², and with all differences between the two wall types being less than 5%.

The above quantitative comparative analyses show that the two walls are significantly equivalent in terms of heat transfer and storage characteristics. Therefore, the subsequent analyses will be uniformly simulated using the 700mm equal thickness geometric model.

3. Results and discussion

3.1 Spatiotemporal evolution of temperature fields in ultra-thick rammed earth walls under bidirectional thermal disturbances

To reveal the spatiotemporal patterns of heat transfer in the

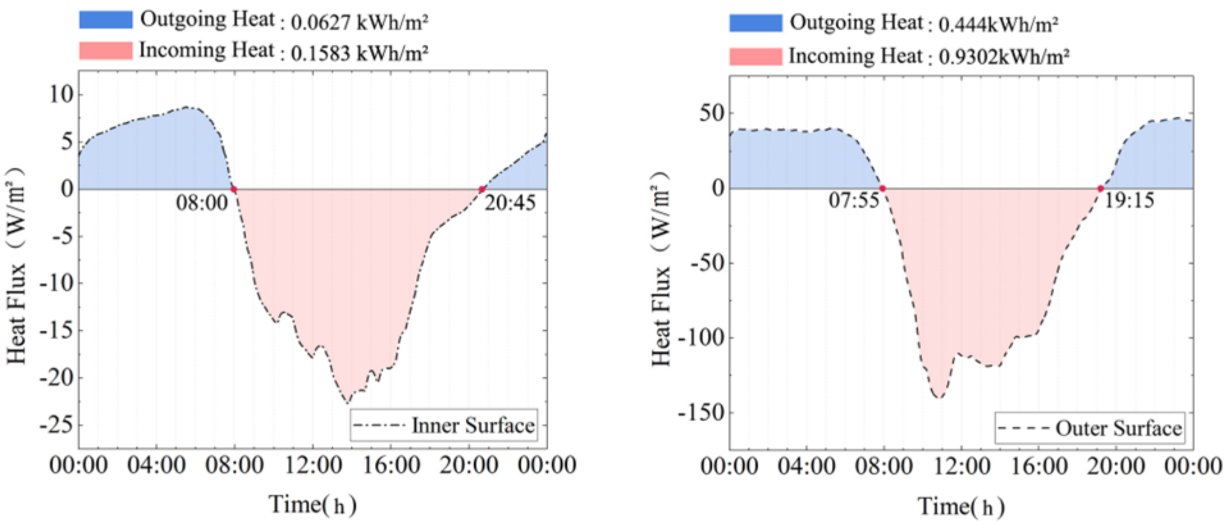

(a) interior surface (b) exterior surface

Fig. 14: Diurnal Variation Patterns of 24-Hour Averaged Heat Flux on Interior and Exterior Surfaces.

wall under bidirectional thermal disturbances, eight temperature monitoring probes were uniformly distributed along the radial depth of the wall (Fig. 9), with Probe1 and Probe8 corresponding to the interior and exterior surfaces, respectively. Based on 48-hour simulated temperature data recorded from these probes (Table S1), spatiotemporal visualization diagrams of the linear temperature field within the wall were constructed (Fig. 10).

Fig. 10(a) initially reveals the time-lag pattern through time-domain fluctuations in probe temperature, while Fig. 10(b) quantifies the temperature decay gradient along the wall depth.

The spatiotemporal temperature field variations of ultra-thick rammed earth walls under bidirectional thermal disturbances, as revealed in Fig. 10, are summarized as follows:

(1) The exterior surface temperature began rising at 06:25 under solar radiation, reaching a daytime peak of 26.01°C at 15:55 before entering the cooling phase. The interior surface temperature started increasing at 06:50 due to indoor thermal fluctuations, peaking at 19.04°C at 16:45. The heating rates differed significantly between surfaces: 0.27°C/h (interior) versus 1.34°C/h (exterior).

(2) All eight probes exhibited pronounced temperature wave time lags and attenuation. Progressive outward-to-inward propagation was observed from Probe8 (exterior) to Probe4, whereas inward-to-outward propagation characterized Probe1 to Probe3. A thermal boundary between external and internal heat sources emerged between Probe3 and Probe5.

(3) The first-cycle temperature wave peaks at Probe3–Probe5 were delayed into the second diurnal cycle (24–48 h).

Preliminary conclusions:

(1) Spatiotemporal thermal transfer heterogeneity arises from bidirectional heat source coupling: Probe8–Probe4 delays are dominated by exterior thermal forcing. Probe1–Probe3 delays are governed by interior thermal forcing. The exterior thermal influence boundary near Probe4 (discussed in-depth later) confirms the wall's strong blocking effect against plateau longwave radiation.

(2) The severe peak delay at Probe3–5 stems from phase interference between external and internal thermal waves. Nonlinear superposition near Probe4 induces periodic heat flux reversals, with energy accumulation amplifying peak delays.

3.2 Temperature attenuation and maximum penetration depth under bidirectional thermal Coupling

The first-cycle temperature fluctuation amplitudes $A_{probe}^{\text{Phase I}}$ for each monitoring point were calculated, followed by the determination of inter-probe temperature attenuation factors $f_{probe}^{\text{Phase I}}$ Eq. (7) (Table 6).

Through analysis of Table 6, the wall can be zonally partitioned based on energy attenuation characteristics and mechanisms under bidirectional thermal disturbances (Fig. 11):

(1) Outdoor Thermal Wave Dominance Zone (0–500 mm): Temperature exhibits outward-to-inward attenuation.

(2) Indoor Thermal Wave Dominance Zone (500–700 mm): Temperature shows inward-to-outward attenuation.

Subzones:

(1) 0–200 mm & 600–700 mm: Governed by outdoor/ indoor thermal waves respectively, with constant attenuation rates ($f = 0.49 - 0.51$) determined by wall thermal inertia and conductivity, where internal thermal wave effects are negligible.

(2) Transition Zone (200–600 mm): Constructive interference of bidirectional thermal waves creates energy accumulation, with attenuation factor decreasing by +0.1

towards 400 mm depth.

Critical findings:

(1) A standing wave energy node forms near 400 mm depth, balancing bidirectional heat flux.

(2) 300–500 mm: Local energy accumulation stabilizes attenuation rate ($f = 0.73$).

To investigate the impact of bidirectional thermal interference on the internal temperature of the wall, we calculated the differences between the extreme temperatures at various depths and the surface temperature (Table S2-S3), and analyzed the temperature difference-depth profile (Fig. 12). The X-axis represents wall depth, the Y-axis denotes temperature differences, and solid/dashed lines indicate differentials relative to exterior/interior surfaces, and colors are used to differentiate the trends of the different temperature extremes.

Fig. 12 reveals spatially heterogeneous characteristics of thermal extremes under bidirectional wave interference:

(1) The exterior-to-interior peak temperature difference increases from 4.85°C to 8.36°C (Table S3), while the interior-to-exterior difference rises from -6.97°C to 1.39°C (Table S2), confirming 0–500 mm as the external thermal wave dominant zone. The reduction from 8.36°C to 6.97°C within 500–700 mm (Table S3) validates internal thermal wave dominance.

(2) The peak temperature of the exogenous heat wave is dominated by the homogeneous attenuation in the interval of 0–300mm, showing a significant temperature decay trend, and in the interval of 300–600mm, the exogenous heat wave is affected by the superposition of the two-way wave and the hysteresis of the standing wave node, and the energy attenuation slows down significantly; the peak temperatures of the external surface are higher than the peak temperatures of the temperature waves inside the wall; the superposition of the two-way wave in the anti-node of 200mm makes the exogenous temperature wave there converge with the internal temperature wave. The two-way wave is superposed at the 200mm antinode, which makes the exogenous temperature wave and the internal surface temperature wave converge, and the peak temperature of the internal surface is approximated to that of the 200mm; in addition, due to the limitation of the gradient of the attenuation factor, the endogenous heat wave can't penetrate into the shallow area of the external surface, which leads to the peak temperature of the internal surface being higher than that in the interval of 200–700mm, and lower than that in the interval of 0–200mm (Fig. 12).

(3) The first cycle valley temperature shows a gentle warming trend from the outside to the inside, and the first cycle valley temperatures of the outer surface are lower than the first cycle valley temperatures of the inner points of the wall. the first cycle valley temperatures tend to stabilize in the interval of 400–700mm under the double influence of the two-way constructive interference and the homogeneous attenuation of the near-inside surface. (Fig. 12)

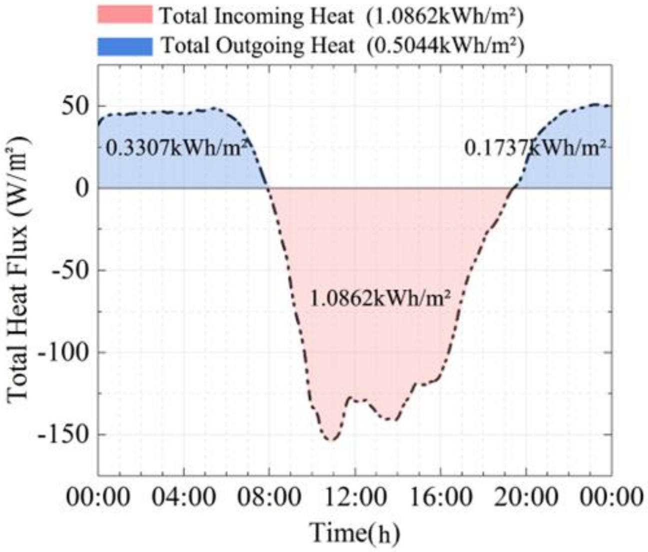

Fig. 15: Overall Thermal Storage and Release Characteristics of Walls.

3.3 Time Lag Characteristics under Bidirectional Thermal Coupling

Using Eq. (6), the time lags $\varphi_{L_{out-in}}$ between three temperature wave extrema (from exterior to interior) and each probe were calculated (Table S4), characterizing the variation trends of time lags for Phase I valley, Phase I peak, and Phase II valley with wall depth (Fig.13). Additionally, the time lag effects k^{peak} and k^{valley} at different depths were defined Eq. (8):

In Fig. 13(c), the X-axis represents the radial depth from the outer wall surface to the inner wall surface; the Y-axis represents the time lag of the temperature wave extremes at different depths. The red solid line is the time lag-depth curve of the first cycle wave peak, the green dashed line is the time lag-depth curve of the first cycle wave valley, and the blue dashed line is the time lag-depth curve of the second cycle wave valley.

Under the interference effects of bidirectional thermal waves from indoor and outdoor environments, the wall's internal temperature extremes exhibit significant time lag-depth differentiation characteristics:

(1) The time lag effects of three temperature extremes (peak/valley) are significantly enhanced within the 100–600 mm depth range. The maximum peak time lag reaches 855 minutes (58.3% of the 24-hour thermal wave cycle), approximately twice the maximum valley time lag (420 minutes), indicating pronounced peak temperature delays. This phenomenon reveals additional time lag effects induced by bidirectional thermal wave interference in the 200–600 mm zone: When external temperature valleys propagate to this

depth, phase superposition of bidirectional waves triggers energy accumulation and thermal oscillations, thereby substantially delaying peak temperature occurrences. Notably, this effect minimally impacts valley time lags due to the weaker thermal influence of valleys compared to peaks.

(2) Peak time lag responses exhibit asymmetric behavior, quantified by the gradient parameter k^{peak}(Table S4):

·0–100 mm: Dominated by exterior surface thermal inertia, weak time lag ($k_{0-100}^{\mathrm{I}\,peak} = 0.9$).

·100–300 mm: Enhanced time lag ($k_{100-300}^{\mathrm{I}\,peak} = 2.65 - 3$) due to thermal diffusion suppression and marginal interference effects.

·300–500 mm: Standing wave node at 400 mm induces critical heat flux reversal, shifting k from positive to negative ($k_{300-500}^{\mathrm{I}\,peak} = 2 - -0.55$).

·500–600 mm: Maximum time lag gradient ($k_{500-600}^{\mathrm{I}\,peak} = -6.95$) occurs as external waves attenuate and internal thermal effects require prolonged equilibration.

·600–700 mm: Interior surface thermal inertia dominance reduces time lag ($k_{600-700}^{\mathrm{I}\,peak} = -0.55$)

(3) Furthermore, within the exterior-source zone at 0–500 mm depth, a Fourier function was applied for functional fitting Eq. (11). In the endogenous zone of 500–700 mm depth, a power function was applied for curve fitting Eq. (12), with the fitting results shown in Fig. 13(a).

$$\Delta t_{peak}(x) = 428.7961 - 426.9522 \cdot \cos(0.0075x) - 45.1138\sin(0.0075x)\ (0 \le x \le 500) \tag{11}$$

$$\Delta t_{peak}(x) = 4.1186 \cdot x^{-10.6381}(500 \le x \le 700) \tag{12}$$

(4) The two valley time lag curves exhibit approximately symmetric dissipative characteristics: Within the shallow 0–400 mm depth range, the energy input from external thermal waves dominates, while internal thermal waves cannot penetrate to this depth. The time lag effects are primarily driven by the linear accumulation of material thermal inertia and bidirectional thermal wave interference effects. A polynomial function was applied to fit the data in the 0–400 mm external source region Eq. (13). Within the endogenous zone (400–700 mm depth range), a polynomial function was applied for data fitting Eq. (14), with the fitting results illustrated in Fig. 13(b).

$$\Delta t_{valley}(x) = 1.0224 \cdot x - 5.0356(0 \le x \le 400) \tag{13}$$

$$\Delta t_{valley}(x) = -1.2661 \cdot x + 895(400 \le x \le 700) \tag{14}$$

3.4 Thermal Storage and Release Characterization under Bidirectional Thermal Coupling

To further investigate the heat storage-release mechanisms of ultra-thick rammed earth walls under bidirectional thermal disturbances, the 24-hour average heat flux dynamics on both interior and exterior surfaces were simulated and monitored (Fig. 14), and the total heat storage-release capacity of the wall was calculated (Fig. 15). In the figures, the X-axis represents the 24-hour simulation time, the Y-axis denotes the average heat flux at wall surfaces, blue areas indicate heat loss, and red areas represent heat gain.

(1) From Interior Surface Heat Storage-Release Characteristics Fig. 14(a):

During nighttime (20:45–08:00), the interior surface continuously releases heat at a total of 0.0627 kWh/m², indicating that the thermal inertia regulation mechanism discharges daytime-stored heat to indoor spaces at night, effectively mitigating the negative impact of low nighttime temperatures on indoor thermal comfort.

During daytime (08:00–20:45), heat transfer into the wall driven by indoor thermal sources reaches 0.1583 kWh/m², demonstrating the dynamic regulation of the wall's heat storage capacity by indoor thermal environments.

(2) From Exterior Surface Heat Storage-Release Characteristics Fig. 14(b):

Nighttime (19:15–07:55) sees the exterior surface dissipating energy via longwave radiation and natural convection, totaling 0.444 kWh/m². This reflects both the enhanced convective heat transfer under plateau low-pressure conditions and the critical role of sky cooling radiation in nighttime heat dissipation.

Daytime (07:55–19:15) features shortwave solar radiation driving the exterior heat flux to a peak of 145W/m², with total heat influx of 0.9302 kWh/m² (85.7% of daytime storage), underscoring solar radiation's dominance in building envelope thermal loads.

(3) Spatial Variability of Heat Flux Amplitudes:

The exterior surface heat flux amplitude reaches 145 W/m² under coupled solar-convective effects, with daytime fluctuation rates (ΔQ/Δt = 7.3 W/m²·h) significantly exceeding nighttime rates (4.1 W/m²·h).

The interior surface, buffered by thermal inertia, exhibits a much lower amplitude of 23.5 W/m² (83.8% reduction compared to exterior), validating the ultra-thick wall's thermal shielding efficacy.

(4) Energy Balance and Dynamic regulatory mechanisms (Fig. 15):

Total daily heat storage: 1.0862 kWh/m² (92.3% concentrated in daytime solar hours); Total heat release: 0.5044 kWh/m²; Net heat storage: 0.5818 kWh/m², confirming the wall's net energy absorption and its capacity to buffer extreme radiation and temperature swings.

Dynamic Regulation Mechanism: The net absorption stems from asymmetric bidirectional thermal fluxes: The daytime outdoor flux (0.9302 kWh/m²) is 5.9 times higher than the indoor flux (0.1583 kWh/m²). The heat released outside at night (0.444 kWh/m²) is 7.1 times higher than the heat released indoors (0.0627 kWh/m²).

This asymmetry enables diurnal solar energy redistribution for nighttime heating, achieving 73.6–77.5% indoor temperature fluctuation attenuation and enhancing passive thermal regulation in plateau buildings.

4. Conclusions and future perspectives

This study overcomes the limitations of conventional models in plateau climate adaptability by developing a transient heat transfer model integrating low atmospheric pressure, intense radiation, and dynamic boundary conditions. We propose the novel concepts of "standing wave node energy accumulation" and "bidirectional wave phase interference," revealing the heat transfer characteristics and dynamic thermal regulation mechanisms of ultra-thick rammed earth walls under coupled bidirectional thermal disturbances in non-steady-state plateau environments. Key findings are:

(1) Spatiotemporal heterogeneity is observed: 0–500 mm depth is dominated by external thermal waves, while 500–700 mm is governed by internal thermal waves. The 0–200 mm and 600–700 mm zones decay at constant rates due to wall thermal inertia, whereas the 200–600 mm transitional interference zone exhibits flattened attenuation.

(2) A standing wave node at 400 mm depth induces periodic heat flux reversal, delaying external temperature wave peaks by 855 minutes (58.3% of the diurnal cycle), Moreover, the fitted function was able to predict the time lag of the temperature extremes at different wall depths.

(3) Asymmetric energy transfer is quantified: daytime heat storage dominates externally (night-time release rate 7.1 times higher than on the internal surface). Net heat storage of 0.5818 kWh/m² verifies the "thermal mass flywheel" effect, converting excess solar energy into nocturnal heating resources, reducing indoor temperature fluctuations by 73.6%–77.5% and buffering diurnal ΔT >23°C.

Based on the theoretical results of this study, the following design recommendations for the wall construction of rammed earth residential buildings in the Shangri-La region are proposed:

(1) Considering the maximum influence depth (500 mm) of external thermal waves under summer natural ventilation conditions, it is recommended that the construction thickness of rammed earth walls should not be less than 500 mm to avoid overheating in summer.

(2) Leveraging the standing wave node characteristics at the 400 mm depth, installing PCM material[35] at the 400 mm depth of rammed earth walls is suggested. This approach maximizes the utilization of PCM material performance, enhances nighttime heat release from the wall to the interior, maintains indoor thermal environment, and constructs a more optimal passive building system.

Notably, this study is based on summer data, and will subsequently extend the winter and transitional season climate parameters to evaluate the thermal performance of rammed earth walls throughout the year; meanwhile, it continues to explore the differences in heat transfer and heat storage of rammed earth walls with different orientations under the plateau climate conditions to further provide a comprehensive theoretical basis for improving the efficiency of thermal regulation under extreme climatic conditions.

Acknowledgements

This research was financially supported by the National Key R&D Program of China (grant No. 2024YFC3808300), the Fundamental Research Funds for the Central Universities in Southwest Minzu University (grant No. ZYN2024158) and the Sichuan Provincial Youth Scientific and Technological Innovation Research Team on Ecological Adaptability of Plateau Architecture (grant No. 2022JDTD0008).
Additionally, the authors acknowledge China-Portugal Joint Laboratory of Cultural Heritage Conservation Science supported by the Belt and Road Initiative.

Conflict of Interest

The authors declare no competing interests.

Supporting Information

Applicable.

Nomenclature

Pr_t	Turbulent Prandtl number [-]
h_{conv}	Convection coefficient [$W/(m^2 \cdot K)$]
T_{sky}	Sky temperature [℃]
P_{ref}	Reference atmospheric pressure [*Kpa*]
ρ	Density [kg/m^3]
c_p	Specific heat capacity [$J/kg \cdot K$]
λ	Thermal conductivity [$W/m \cdot K$]
μ	Dynamic viscosity [$Pa \cdot s$]
ϵ	Surface emissivity [-]
RMSE	Root mean square error [℃]
R^2	Coefficient of determination [-]
Mean AE	Mean absolute error [℃]
Max AE	Maximum absolute error [℃]
PD	Phase difference [*min*]
PTD	Peak time difference [*min*]

f	Attenuation factor [-]
φ	Time lag [min]
$f_{probe}^{\text{Phase I}}$	Attenuation factor [-]
k^{peak}	Time lag effect [-]
L^{deep}	Maximum impact depth [mm]

CRediT Statement

Junjia Hu: Conceptualization; Data curation; Formal analysis; Funding acquisition; Investigation; Methodology; Software; Supervision; Validation; Visualization; Writing-original draft; Writing-review & editing. **Xiaoliang Wang:** Conceptualization; Data curation; Formal analysis; Funding acquisition; Investigation; Methodology; Project administration; Resources; Software; Supervision; Validation; Writing-review & editing. **Li Yang:** Funding acquisition; Investigation; Methodology; Project administration; Supervision; **Shuliang Li:** Funding acquisition; Investigation; Methodology; Project administration; Supervision. **Yunke Yang:** Investigation; Methodology; Software. **Yuzhenru Sun:** Investigation; Methodology. **Yong Sha:** Investigation; Methodology. **Guanxing Pu:** Investigation; Methodology; Software. **Xianmin Mai:** Funding acquisition; Investigation; Methodology; Project administration; Resources; Software; Supervision; Validation; Visualization; Writing-review & editing.

References

[1] United Nations Framework Convention on Climate Change (UNFCCC), The Paris Agreement (2021). In: *Proceedings of UN Climate Change Conference*; 2021 Oct 31–Nov 13; Glasgow, Scotland. New York City: UNFCCC.

[2] O. Kaynakli, A review of the economical and optimum thermal insulation thickness for building applications, *Renewable and Sustainable Energy Reviews*, 2012, **16**, 415-425, doi: 10.1016/j.rser.2011.08.006.

[3] K. Parvin, M. J. Hossain, A. Z. Arsad, P. J. Ker, M. A. Hannan, Building energy technologies towards achieving net-zero pathway: A comprehensive review, challenges and future directions, *Journal of Building Engineering*, 2025, **100**, 111795, doi: 10.1016/j.jobe.2025.111795.

[4], L. Lu, T. Zhang, X. Wang, Y. Han, D. Sridhar, H. Li, B. B. Xu, K. V. Fedorovich, X. Mai, Evaluation and analysis of the architectural environment of traditional folk houses in Tibetan Plateau, China, *Engineered Science*, 2023: **22**, doi: 10.30919/es8d845

[5] X. Wang, X. Mai, B. Lei, H. Bi, B. Zhao, G. Mao, Collaborative optimization between passive design measures and active heating systems for building heating in Qinghai-Tibet plateau of China, *Renewable Energy*, 2020, **147**, 683-694, doi: 10.1016/j.renene.2019.09.031.

[6] X. Wang, Y. Wu, X. Dong, M. Liu, B. Lei, X. Mai, Optimization of global energy consumption of buildings based on photothermal coupling effect of exterior windows in Qinghai-Tibet plateau, *Journal of Building Engineering*, 2024, **85**, 108710, doi: 10.1016/j.jobe.2024.108710.

[7] M. A. Martin-Antunes, C. Perlot, S. Espuelas, S. Marcelino, A. Seco, Recent developments in stabilized rammed earth: Testing protocols and the recommendations for standardization, *Journal of Building Engineering*, 2025, **106**, 112436, doi: 10.1016/j.jobe.2025.112436.

[8] Á. Fernando, E. Puertas, R. Gallego, Characterization of the mechanical and physical properties of stabilized rammed earth: A review, *Construction and Building Materials*, 2022, **325**, 126693, doi: 10.1016/j.conbuildmat.2022.126693.

[9] Á. Fernando, E. Puertas, R. Gallego, Characterization of the mechanical and physical properties of unstabilized rammed earth: A review, *Construction and Building Materials*, 2021, **270**, 121435, doi: 10.1016/j.conbuildmat.2020.121435.

[10] Liu, X. Architectural Physics, Beijing: China Architecture & Building Press, ed. Fourth Edition, 2024, 516, ISBN 9787112291991. (in Chinese)

[11] H. Asan, Effects of wall's insulation thickness and position on time lag and decrement factor, *Energy and Buildings*, 1998, **28**, 299-305, doi: 10.1016/S0378-7788(98)00030-9.

[12] H. Asan, Y. S. Sancaktar, Effects of Wall's thermophysical properties on time lag and decrement factor, *Energy and Buildings*, 1998, **28**, 159-166, doi: 10.1016/S0378-7788(98)00007-3.

[13] H. Asan, Numerical computation of time lags and decrement factors for different building materials, *Building and Environment*, 2006, **41**, 615-620, doi: 10.1016/j.buildenv.2005.02.020.

[14] X. Jin, X. Zhang, Y. Cao, G. Wang, Thermal performance evaluation of the wall using heat flux time lag and decrement factor, *Energy and Buildings*, 2012, **47**, 369-374, doi: 10.1016/j.enbuild.2011.12.010.

[15] C. R. Ruivo, P. M. Ferreira, D. C. Vaz, On the error of calculation of heat gains through walls by methods using constant decrement factor and time lag values, *Energy and Buildings*, 2013, **60**, 252-261, doi: 10.1016/j.enbuild.2013.02.001.

[16] D. Mazzeo, G. Oliveti, N. Arcuri, Influence of internal and external boundary conditions on the decrement factor and time lag heat flux of building walls in steady periodic regime, *Applied Energy*, 2016, **164**, 509-531, doi: 10.1016/j.apenergy.2015.11.076.

[17] Y. Lu, L. Wang, J. He, R. Yang, L. Yuan, Dimensionless resolutions for heat flux decrement factor and time lag of the wall during cyclic variations in outdoor air temperature, *Case Studies in Thermal Engineering*, 2024, **60**, 104678, doi: 10.1016/j.csite.2024.104678.

[18] S. A. Al-Sanea, M. F. Zedan, S. N. Al-Hussain, Effect of thermal mass on performance of insulated building walls and the concept of energy savings potential, *Applied Energy*, 2012, **89**, 430-442, doi: 10.1016/j.apenergy.2011.08.009.

[19] T. Pekdogan, T. Basaran, Thermal performance of different

exterior wall structures based on wall orientation, *Applied Thermal Engineering*, 2017, **112**, 15-24, doi: 10.1016/j.applthermaleng.2016.10.068.

[20] L. Hou, Y. Liu, Y. Zhu, L. Liu, X. Zhao, L. Yang, Thermal performance of cavity masonry wall structures in the solar rich areas of Western China, *Journal of Building Engineering*, 2024, **86**, 108797, doi: 10.1016/j.jobe.2024.108797.

[21] Corrado Vincenzo, Gorrino Alice, Paduos Simona, Energy performance characterisation of vented opaque envelope through simplified methodologies, *Journal of Building Simulation Applications,* (2013), (BSA 2013) 2013-january: 323-332.

[22] V. Corrado, S. Paduos, New equivalent parameters for thermal characterization of opaque building envelope components under dynamic conditions, *Applied Energy*, 2016, **163**, 313-322, doi: 10.1016/j.apenergy.2015.10.123.

[23] N. C. Balaji, M. Mani, B. V. Venkatarama Reddy, Dynamic thermal performance of conventional and alternative building wall envelopes, *Journal of Building Engineering*, 2019, **21**, 373-395, doi: 10.1016/j.jobe.2018.11.002.

[24] F. Leccese, G. Salvadori, F. Asdrubali, P. Gori, Passive thermal behaviour of buildings: performance of external multi-layered walls and influence of internal walls, *Applied Energy*, 2018, **225**, 1078-1089, doi: 10.1016/j.apenergy.2018.05.090.

[25] P. K. S. Rathore, S. K. Shukla, N. K. Gupta, Yearly analysis of peak temperature, thermal amplitude, time lag and decrement factor of a building envelope in tropical climate, *Journal of Building Engineering*, 2020, **31**, 101459, doi: 10.1016/j.jobe.2020.101459.

[26] Coleman, Hugh & Members, Committee. ASME V&V 20-2009, Standard for Verification and Validation in Computational Fluid Dynamics and Heat Transfer, The American Society of Mechanical Engineers, New York, (V&V20 Committee Chair and principal author).

[27] X. Hu, H. Zhang, H. Yu, Numerical simulation study on the hygrothermal performance of building exterior walls under dynamic wind-driven rain condition, *Building Simulation*, 2024, **17**, 207-221, doi: 10.1007/s12273-023-1076-3.

[28] T. Yamamoto, A. Ozaki, S. Kaoru, K. Taniguchi, Analysis method based on coupled heat transfer and CFD simulations for buildings with thermally complex building envelopes, *Building and Environment*, 2021, **191**, 107521, doi: 10.1016/j.buildenv.2020.107521.

[29] The U.S. Department of Energy (DOE)/NREL/ALLIANCE, National Renewable Energy Laboratory, SOLPOS – Solar Calculator. http://rredc.nrel.gov/solar/codesandalgorithms/solpos/

[30] J. A. Duffie, W. A. Beckman, J. McGowan, Solar engineering of thermal processes, *American Journal of Physics*, 1985, **53**, 382, doi: 10.1119/1.14178.

[31] The People's Republic of China National Standard GB 50176-2016, (2016). Code for Thermal Design of Civil Building, China Architecture and Building Press, Beijing. (in Chinese)

[32] Engineering Tool Box [online] (2001). Available at: https://www.engineeringtoolbox.com. (Accessed25 March 2024).

[33] S. E. Chorfi, G. El Guermai, L. Maniar, W. Zouhair, Numerical identification of initial temperatures in heat equation with dynamic boundary conditions, *Mediterranean Journal of Mathematics*, 2023, **20**, 256, doi: 10.1007/s00009-023-02461-8.

[34] The People's Republic of China Industry Standard JGJ/T347-2014, (2014). Standard of Test Methods for Thermal Environment of Building, China Architecture and Building Press, Beijing. (in Chinese)

[35] Z. Liu, Z. J. Yu, T. Yang, D. Qin, S. Li, G. Zhang, F. Haghighat, M. M. Joybari, A review on macro-encapsulated phase change material for building envelope applications, *Building and Environment*, 2018, **144**, 281-294, doi: 10.1016/j.buildenv.2018.08.030.

Publisher's Note: Engineered Science Publisher remains neutral with regard to jurisdictional claims in published maps and institutional affiliations.

Open Access